Quantitative density retrieval of gas jets for high harmonic generation EUV sources with a compact schlieren imaging system

Weerdenburg, Sven; Horsten, Roland; Coene, Wim

DOI
10.1364/AO.553974

Publication date
2025

Document Version
Final published version

Published in
Applied Optics

Citation (APA)
Weerdenburg, S., Horsten, R., & Coene, W. (2025). Quantitative density retrieval of gas jets for high harmonic generation EUV sources with a compact schlieren imaging system. *Applied Optics*, *64*(14), 3871-3879. https://doi.org/10.1364/AO.553974

Research Article Vol. 64, No. 14 / 10 May 2025 / Applied Optics 3871

applied optics

Quantitative density retrieval of gas jets for high harmonic generation EUV sources with a compact schlieren imaging system

Sven Weerdenburg,[1,*] Roland Horsten,[1] and Wim Coene[1,2]

[1]Optics Research Cluster, ImPhys Department, Delft University of Technology, Delft, The Netherlands
[2]ASML Research, Veldhoven, The Netherlands
*s.weerdenburg@tudelft.nl

Received 2 January 2025; revised 16 February 2025; accepted 19 February 2025; posted 25 February 2025; published 21 March 2025

We demonstrate the implementation of a compact schlieren imaging technique for quantitatively measuring atomic density profiles in a gas jet-based high harmonic generation EUV source. This technique compares high harmonic generation light sources and optimization, considering different nozzle geometries, backing pressures, and vacuum systems. The simplicity of schlieren imaging could make it a suitable standardized inspection tool for gas jet-based high harmonic generation sources. Several gas jet profiles at different backing pressures were analyzed, enabling the retrieval of the peak pressure within the gas jet and the impact of the vacuum system on the jets' shape.

https://doi.org/10.1364/AO.553974

1. INTRODUCTION

High-order harmonic generation (HHG), driven by high-power laser systems, has seen impressive advancements in recent years [1,2]. The typical low efficiency of HHG in the EUV and soft x-ray regime led to the need for more powerful drive lasers with shorter pulse duration. The introduction of, for example, chirped pulse amplification (CPA) [3], high pulse energy femtosecond lasers (such as titanium sapphire lasers), and more recently, the availability of commercial ytterbium-doped fiber lasers [4–8], has enabled the generation of coherent extreme ultraviolet (EUV) light with output power up to the milliwatt range [7,9–11]. This power is sufficient for scientific applications such as coherent imaging [1,12–15], spectroscopy [16], and even industrial applications [17]. Despite these advancements, there is still a demand for higher photon fluxes to improve acquisition times and system stability, which calls for further optimization efforts in HHG-based EUV sources.

The HHG process results from the response of a single atom to the electric field from the drive laser distorting the potential field of the atom. From the semi-classical point of view (using the three-step model), the electron of the parent atom ionizes through tunneling and gains kinetic energy [18–20]. Maximum energy, defined by ponderomotive energy, is mainly relevant for maximum photon energy. This ponderomotive energy depends on the wavelength and pulse energy of the drive laser [21]. On the macroscopic scale, a collection of single atoms needs to emit the generated higher harmonics coherently through phase matching. Phase matching is a balancing process of induced phase mismatch due to focusing geometry, dipole phase, or the refractive index by the medium and plasma [22]. The focusing geometry of the drive lasers and the medium length within the field combined with the atomic density strongly affect the phase-matching conditions [21,23–25]. In particular, the focusing geometry becomes of importance for ytterbium-doped fiber lasers with their relatively low energy pulses, which requires tighter focusing and therefore a strong phase profile. Optimizing the phase-matching conditions results in a higher output of coherent harmonics and therefore an improved conversion efficiency, limited by the reabsorption of higher harmonics by the gas medium [21,26].

Although there is a continuous better theoretical understanding of the optimal geometry for the medium and focusing of the drive laser [19], a wide range of HHG systems are available and are not that trivial to compare. They vary from low-pressure capillaries [27–29] and cells [30,31] to both pulsed and continuous high-pressure gas jets [32,33]. Note that higher harmonics can also be produced in solids and liquids [34–36], but gas-based systems are more common due to their relatively higher photon fluxes, higher photon energies, and relative simplicity. In this work, we focus on gas jet-based systems.

In order to make a comparison between different light sources and their efficiency, it would be desired to compare the number of atoms that interact with the laser field. Therefore, there is a need to retrieve the medium volume and atomic density in a given HHG system. Defining the medium length in capillaries

and low-pressure cells is rather straightforward as the dimensions are known. On top of that, as the gas is contained within a volume and is a rather static system, the pressure can be directly measured with a pressure gauge. For gas jets, however, this can be a bit more of a challenge as the gas is freely injected into a vacuum system and, therefore, not enclosed within a well-defined volume. The pressure profile within the medium depends on the nozzle geometry, the backing pressure, and the presence of a gas catcher placed opposite the gas nozzle, which could potentially influence the profile depending on its placement and pumping efficiency. As these can differ significantly per HHG system, it makes it hard to compare systems with only the knowledge of the backing pressure.

Interferometry-based methods are able to retrieve the density due to the introduced optical path difference caused by the difference in the refractive index of the gas jet [21,37–40]. However, interferometry approaches can be quite tricky to implement due to vibrations introduced through the scroll pumps, turbo molecular pumps, and gas line feeding the gas jet itself.

A different approach has been proposed [41], which associates the observed plasma intensity with a set of reference measurements. First, the vacuum chamber is saturated to a certain pressure of interest, i.e., there is no gas jet but an increased static pressure. A plasma is created at this static pressure, and an image is acquired. The peak brightness of the plasma is associated with the static pressure. This is repeated for a set of pressures to populate a look-up table (LUT), which can be used to reference the observed plasma intensity with the LUT during HHG. Although this approach circumvents interferometry, it has quite a few limitations. First, a technical inconvenience: if a pressure above 1 bar is desired, one would have to saturate the entire vacuum chamber to a positive pressure difference. Most vacuum chambers (especially those with glass windows) are not designed for positive pressure differences and could therefore damage the vacuum system. On a more fundamental level, this approach requires accurate knowledge of the intensity profile of the laser and its spatial profile, as it is hard to differentiate changes in laser power or change in pressure in the gas jet. On top of that, this calibration process has to be repeated as soon as the settings of the drive laser have been changed.

In this work, we demonstrate a compact method, based on schlieren imaging, to retrieve the atomic density profile in a gas jet-based HHG source, which could potentially be used in further studies as an input for further studies on phase matching and optimization of the efficiency of HHG light sources.

2. SCHLIEREN IMAGING

Schlieren imaging systems have been widely applied to visualize fluctuations in the density of gases, from the aerodynamics of airplanes [42] to gas flows in industrial applications [43]. This technique exploits the fact that the density of these gases ρ affects the refractive index n of the medium, described by the Gladstone–Dale (GD) relation [44]:

$$n = \kappa\rho + 1. \tag{1}$$

The κ factor in Eq. (1) represents the Gladstone–Dale constant of a particular gas, which equals $0.1567 \cdot 10^{-3}$ m^3 per kg for argon at 633 nm [45,46]. In a gas mixture, the total refractive index is calculated by summing the contributions of each individual gas, each characterized by its own specific term $\kappa_i\rho_i$. An overview of Gladstone–Dale constants of the relevant gases for HHG can be found in Table 1, reproduced from Ref. [46].

A plane wavefront approaches an object characterized by a spatially varying refractive index. To simplify the analysis [47], we assume a constant refractive index gradient across the object, where the refractive index at position x_1 is higher than that at position x_2. Specifically, the refractive index at the bottom of the object, denoted as n_1, is greater than the refractive index at the top, denoted as n_2. As a consequence of this gradient, light propagates at different speeds within the object: the light at the top, where the refractive index is lower (n_2), travels faster than the light at the bottom, where the refractive index is higher (n_1). This difference in propagation speeds causes the wavefront to tilt, denoted as $\Delta\varepsilon$. The introduced deflection angle $\Delta\varepsilon$ can be geometrically derived (Fig. 1):

$$\Delta\varepsilon = \frac{c/n_2 - c/n_1}{\Delta x}\Delta t \quad \text{with} \quad \Delta t = \Delta z\frac{n}{c}, \tag{2}$$

where n represents the refractive index at an arbitrary point between x_1 and x_2 in the medium at position z_2, and Δz represents the distance between point z_1 and z_2. After simplification, we get

$$\Delta\varepsilon = \frac{n}{n_1 n_2}\frac{n_1 - n_2}{\Delta x}\Delta z. \tag{3}$$

By taking the limit where the differences ($\Delta\varepsilon$, Δn, Δx, and Δz) become infinitesimally small, the equation simplifies to

$$\frac{\partial\varepsilon}{\partial z} = \frac{1}{n}\frac{\partial n}{\partial x}. \tag{4}$$

In order to retrieve the total induced angle deviation by an object with a thickness z, we have to integrate along the z axis:

$$\varepsilon = \frac{1}{n}\int \frac{\partial n}{\partial x}\mathrm{d}z. \tag{5}$$

This equation is the mathematical basis for schlieren imaging [47]. For a 2D schlieren object of length z with a constant gradient for the refractive index, this integral can be simplified by multiplying the gradient with the total length, similar to the case in the example in Fig. 1. However, this is not a case that is often practical. For axis-symmetric schlieren objects, such as gas jets, an Abel transform [43,48] can be applied. For more complex targets, where volumetric atomic densities are of interest, a tomographic Radon approach [49–51] is needed where schlieren images at multiple viewing angles around the target are required. This is outside the scope of the work presented here.

In a schlieren imaging system, this behavior, as described by Eq. (5), is exploited by either blocking or allowing the refracted light rays to pass, creating contrasts that correlate with the gradient of the refractive index. The simplest form is illustrated in Fig. 1, where the light beam that is deflected moves away from the knife edge, passing more photons, thus resulting in a brighter point. In this way, the degree of deflection can be visualized as a gray scale image $C(x)$:

Table 1. Overview of Gladstone–Dale Constants of Gases That Are Relevant for High Harmonic Generation Sources[a]

Gas-Type	Ne	Ar	Kr	Xe	He	H_2	N_2
Gladstone–Dale constant [cm^3/g]	0.0740	0.1567	0.1135	0.1174	0.1928	1.538	0.2378

[a]The values are reproduced from Ref. [46].

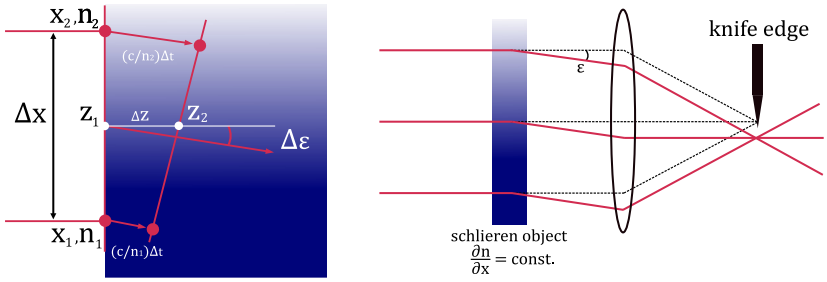

Fig. 1. **Left:** a plane wavefront approaches an object with a varying refractive index. For simplicity, we take a constant gradient across the object where the refractive index at x_1 is higher compared to x_2. Due to the lower refractive index n_2 at the top, the light propagates faster at the top compared to the light at the bottom with a higher refractive index n_1. This results in a tilted wavefront with an angle $\Delta\varepsilon$. The figure is an adapted version from [47]. **Right:** a schlieren imaging system introduces a contrast by adding a knife edge in the beam path, either passing less or more photons. In the example figure, where we have a target where the gradient in the refractive index is constant, the beam gets deflected, resulting in a bright image.

$$C(x) \propto S \int \frac{\partial n}{\partial x} \mathrm{d}z, \tag{6}$$

with S being the sensitivity of the schlieren system. Therefore, this suggests that the schlieren methodology is a relatively simple and straightforward approach for the metrology of gas flows.

3. HIGH HARMONIC GENERATION EUV BEAMLINE WITH INTEGRATED COMPACT SCHLIEREN IMAGING SYSTEM

In this work, we apply the imaging system on a gas jet-based HHG source. The HHG source [7] is driven by a Ytterbium-doped fiber laser with a center wavelength at 1030 nm at a repetition rate of 600 kHz and set to at an average power of 50 W before temporal pulse compression. After (nonlinear) pulse compression by a krypton-filled hollow core fiber, with a power efficiency of 68%, and a set of chirped mirrors to a pulse duration of 38 fs, the light is focused into a vacuum chamber with a plano-convex lens of 80 mm to a focus spot of 21 µm resulting in a peak intensity of $4.3 \cdot 10^{14}$ W/cm^2. The focus is placed between a copper nozzle piece with an opening aperture of 300 µm and a gas catcher. The nozzle is pressurized with argon up to 10 bar. A gas catcher is placed on the opposite side of the nozzle about 400 µm away. The gas catcher is directly attached to a scroll pump to ensure that the vacuum level maintains below 10^{-2} mbar when the argon gas is injected into the vacuum system. An ambient pressure of 10^{-6} mbar is reached without gas injection.

When the argon gas jet interacts with the high-power infrared laser, as shown in Fig. 3, a plasma forms in which higher harmonics up to the EUV regime are produced. These harmonics then travel to a second vacuum chamber, where the driving laser is separated from the extreme ultraviolet (EUV) light through a set of Brewster mirrors. Any residual IR light is blocked by an aluminum foil of 200 nm thickness. The resulting EUV light can be analyzed using an offline EUV spectrometer, as illustrated in a 3D rendering in Fig. 2.

To obtain the density profile of the gas jet in the HHG system, a schlieren system has to be implemented perpendicular to the infrared (IR) beam and the gas jet. Common designs for schlieren imaging include the Toepler double lens system [52] and the Z-type schlieren system [43,53], which uses two parabolic mirrors. These methods utilize a collimated beam to illuminate the schlieren object, with the light passing through the object only once. The second lens in these setups is used to form an image of the light source at the location of a knife edge. Then a camera equipped with an objective lens captures the image of the object.

However, these configurations require a vacuum chamber equipped with two aligned windows (entry and exit windows), which is not present in the current vacuum chamber. Integrating a standard single-pass schlieren system in such a system is not an option. Therefore, a double-pass, single-optic schlieren system, as shown in Fig. 2, is chosen instead [43]. This alternative approach is more feasible for the existing vacuum chamber configuration, and double passing the jet enables higher sensitivity or a smaller form factor [37].

A spherical mirror with a focal length of 250 mm is placed just below the gas jet and gas jet system in the vacuum chamber. Note that this is significantly shorter compared to a typical schlieren system where optics in the order of meters are not uncommon [54–56]. Longer focal lengths enhance the sensitivity to angular deflection, as a small deflection results in relatively larger displacements over longer distances. In our case, a spherical mirror with a focal length of 250 mm is the largest that could be accommodated in the system. The mirror is not mounted and rests on the bottom plate of the chamber. The mirror is illuminated close to normal incidence with a monochromatic LED light source ($\lambda = 625$ nm), which is placed outside the vacuum chamber. The back reflected light by the spherical mirror leaves the vacuum chamber through the same window where an

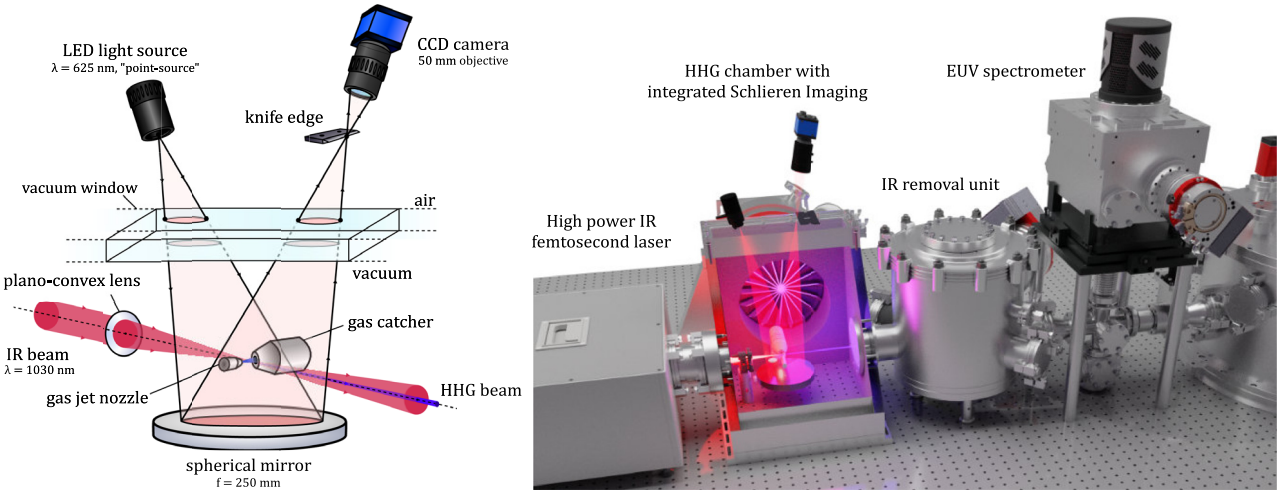

Fig. 2. **Left:** a schematic overview of the compact schlieren imaging setup within a high harmonic generation vacuum chamber. The drive laser is focused between the gas jet nozzle and gas catcher, resulting in a plasma where the higher harmonics are generated. A spherical mirror with a focal length of 250 mm is placed just below the gas jet, which is illuminated by an LED light source that acts as a "point source." The back-reflected light forms an image of the light source outside the vacuum chamber, where a knife edge is placed. A CCD camera with a 50 mm objective and two times extender captures the light and is focused onto the gas jet. **Right:** a 3D render of the setup with a cross section of the schlieren setup, showing the cross section within the vacuum chamber. The generated harmonics propagate to the next vacuum chamber, where the drive laser is separated from the EUV light. The generated EUV light can be inspected with an offline EUV spectrometer.

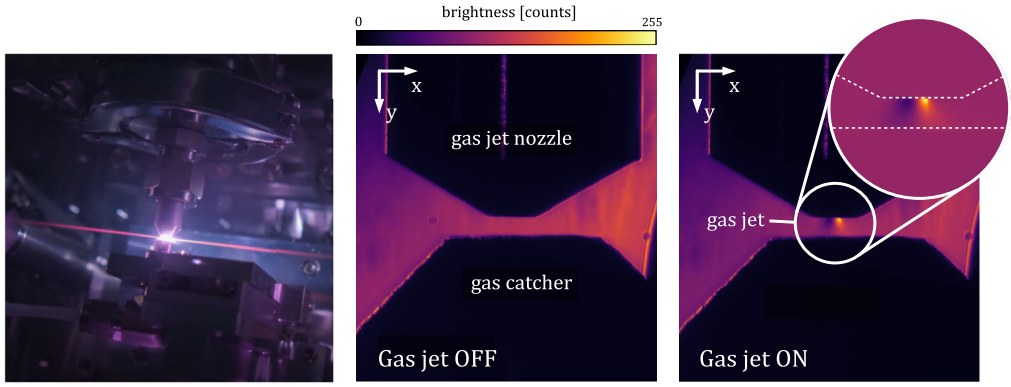

Fig. 3. **Left:** the high-power IR beam is focused between the gas jet nozzle and the gas catcher, leading to a plasma that can be observed through the vacuum window. **Center:** in the schlieren imaging system, we focus on the gas catcher and gas jet nozzle. The background is not uniform due to slightly non-uniform illumination. This can be corrected by subtracting a background image, i.e., a reference image without a gas target. **Right:** when the gas jet is turned on, a contrast can be observed. The contrast can be enhanced and corrected for inhomogeneities in the background by subtracting the background image as shown in the circular inset. The dashed lines indicate the location of the nozzle and gas catcher.

image is formed of the LED source. At this point, a knife edge is placed parallel with the gas jet to create contrast perpendicular to the gas jet, as shown in Fig. 2. A CCD camera (SVS-Vistek ECO445M) with a 50 mm camera objective (Edmund Optics F2.0/50 mm 59873) combined with a C-mount 2× extender (Computar EX2C) is focused onto the gas jet and gas catcher assembly. A schematic overview of the system can be found in Fig. 2. systems that have a relatively small window size can implement a beam splitter between the LED light source and the camera to illuminate the mirror at normal incidence. This approach comes at the cost of a reduced intensity captured by the camera.

4. RESULTS

As shown in Fig. 3, the schlieren camera captures both the gas jet nozzle (at the top of the field of view) and the gas catcher (at the bottom of the field of view) after a manual rotation and cropping of the raw image. When argon is injected into the vacuum chamber, a contrast can be observed between the nozzle and catcher, as illustrated in Fig. 3. To compensate for the uneven background, a series of 500 reference images were captured in the absence of any gas, i.e., background frames. These images have been averaged and subtracted from the frames that contain the gas jet, isolating the schlieren contrast. See the insets in Figs. 3 and 5.

The gray values measured by the imaging system are proportional to the gradient of the refractive index in the gas jet via the induced deflection angle ε. The retrieved gray values are not intrinsically quantitative, as the contrast is also dependent on system-specific parameters such as knife edge placement and focal lengths of the used optics. Calibration of these gray values can be achieved, following the method proposed by Hargather and Settles [57], by placing a weak lens at the same plane as the gas jet. The weak lens refracts the light ray at a defined angle ε as

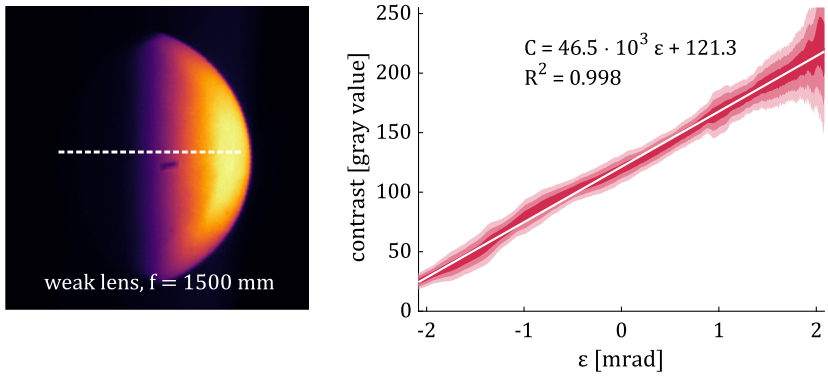

Fig. 4. A weak lens, with a focal length of 1500 mm, is placed in the field of view of the schlieren imaging system. A linear gradient can be observed across the lens due to the introduced angular deflection. With a known focal length of the lens, a measured contrast or gray value C can be associated with an introduced deflection angle ε in order to calibrate the schlieren imaging system.

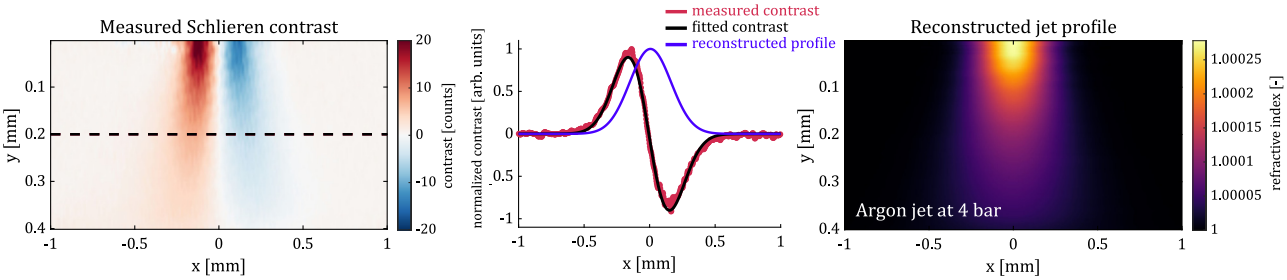

Fig. 5. **Left:** a knife is placed parallel to the gas jet to visualize the gradient perpendicular to the knife, i.e., the gradient proportional to the refractive index of an argon gas jet in the x direction. **Center:** the derivative of a Gaussian function is fitted (indicated by the black line) in the measured contrast (indicated by the red line). Using the retrieved parameters, a Gaussian profile can be reconstructed as indicated by the purple line. **Right:** this process is repeated for the entire gas jet length. After an inverse Radon transform combined with the sensitivity of the schlieren system, the refractive index of the gas jet is reconstructed.

$$\tan \varepsilon = \frac{r}{f} \approx \varepsilon, \tag{7}$$

where r represents a radial point within the lens aligned with the knife edge, and f is the focal length of the weak lens. In the vacuum chamber of the HHG source, a lens with a diameter of 12.7 mm and a focal length of 1500 mm is placed, as shown in Fig. 2. By applying Eq. (7) along with the focal length and radius of the lens, the dynamic range of the schlieren system can be determined if the full dynamic range of the camera is utilized. This results in a maximum calibration range of ±4.2 mrad. It must be noted that the focal length of the calibration lens is taken from the supplier specifications given for 580 nm. Due to chromatic aberration, the actual focal length for 625 nm is slightly different, which introduces a systematic uncertainty. The placement of the knife edge, the amount of light cut off, the source power, and the dynamic range of the camera determine the system's dynamic range.

A set of 500 images was captured of the weak lens in the schlieren system with an exposure time of 5 ms and averaged. A linear response along the x direction, perpendicular to the knife edge, is observed in the schlieren image, as shown in Fig. 4. The response is fitted with a linear function to retrieve a calibration contrast curve C to convert the gray values to deflection angles, where the slope defines the sensitivity S. The actual dynamic range and resolution of the schlieren system, as shown in Fig. 4, is ±2.1 mrad with a resolution of 16.5 µrad, respectively, considering a relatively low dynamic range of the CCD camera (8-bit). With an angular resolution of 16.5 µrad and dynamic range of ±2.1 mrad in combination with Eq. (4), a sensitivity and a dynamic range of the refractive index gradient can be approximated to $10^{-8}\ \mu m^{-1}$ and $2.1 \cdot 10^{-2}\ \mu m^{-1}$. respectively. While a longer focal length of the spherical mirror would improve the sensitivity, the current configuration provides sufficient resolution for retrieving the density while maintaining compatibility with the experimental vacuum chamber constraints.

A schlieren contrast is measured for an argon gas jet with a backing pressure of 4 bar, as shown in Fig. 5. An indication of the shape of the density profile can be retrieved by numerically integrating the measurements along the x axis, as schlieren visualizes the gradient of the refractive index or the atomic density [Eq. (5)]. In this case, the profile shows features of a Gaussian-like profile in the x direction, as observed in other works with similar nozzle geometries [58,59]. Instead of integrating the data itself, the first-order derivative of a Gaussian is fitted to the data. This is used to reconstruct a fitted Gaussian profile and is repeated for each line in the y direction in the measured dataset, yielding a fully reconstructed jet profile, as shown in Fig. 5. This approach serves as a smoothing method to reduce noise artifacts while retrieving a continuous density distribution. While Gaussian profiles are commonly observed in gas jet expansions, we acknowledge that this imposes a functional assumption on the profile.

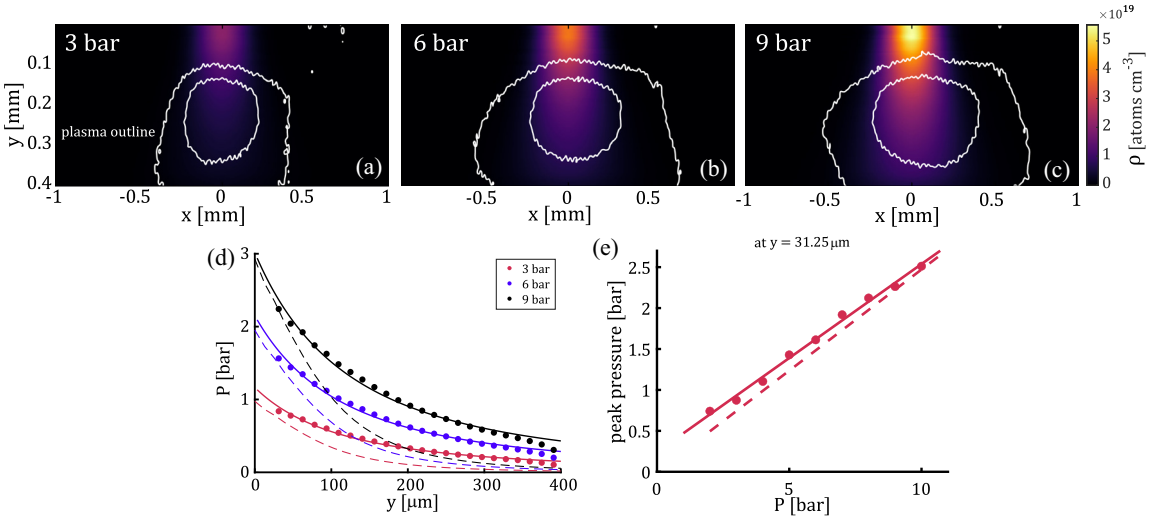

Fig. 6. **Top row:** reconstructed density profiles in atoms per cm^3 of an argon gas jet with a nozzle backing pressure of 3, 6, and 9 bar. The white outlines indicate the size of the observed plasma at a given backing pressure when the gas jet is exposed to the fundamental drive laser. The center white outline indicates the half of the observed peak plasma brightness (FWHM), and the second outline refers to the $1/e^2$ value of the peak brightness. **Bottom row:** the peak pressure in the retrieved gas jet pressure profile drops off exponentially starting from the gas jet nozzle at $y = 0$. The maximum measured peak pressure within the entire gas jet (measured at 31 μm after the observable edge of the nozzle), increases linearly with the backing pressure behind the nozzle. In Figs. 6(d) and (e), the dashed lines represent the simulated pressure distribution of a simple nozzle case conducted in COMSOL. The peak values at the nozzles exit compare quite well with the simulations; however, the peak pressure drops quicker in the COMSOL simulations; see Supplement 1 and the underlying model in Dataset 1, Ref. [67]. The gas jet expands further in the horizontal direction (x direction) compared to what has been observed in the schlieren measurements.

The light propagates through the gas jet, which has a certain thickness along the z axis. The measured contrast corresponds to a projection function of the refractive index gradient. In the case of an axis-symmetric gas flow, it is common to apply the Abel inversion transform [37,60–63]. This transform is used to retrieve the radial profile of the gas jet from the projection. The Abel inversion transform is defined as

$$n(r) - n_0 = \frac{1}{S}\int_r^\infty \frac{C(x)}{\pi\sqrt{x^2 - r^2}}\mathrm{d}x, \tag{8}$$

where n_0 is the ambient refractive index (assumed to be one), r is the radial location in the jet, x is the horizontal location in the projection, and C is the measured contrast. The Abel transform and its inversion are linked to the Radon transform, where the Radon transform does not have the axis symmetry requirement [64,65]. Although the Radon transform is a bit excessive for this application, it is generally better supported in software packages such as Matlab [66]. The inverse Radon transform has therefore been utilized instead. This approach successfully led to the reconstruction of the refractive index profile, as depicted in Fig. 5. With a backing pressure of 4 bar, the peak refractive index retrieved in the jet is 1.00028, which corresponds to approximately 1.07 bar, using the Gladstone–Dale relation [see Eq. (1)] measured at 31 μm away from the nozzle. This compares well with the value found in a computational fluid dynamics (CFD) model in COMSOL, where a pressure of 0.98 bar has been found; see Supplement 1 and Dataset 1, Ref. [67]. The pressure can be converted to an atomic density by using the ideal gas law (assuming room temperature) and the molar mass of argon. This methodology has been repeated for backing pressures from 2 up to 10 bar with steps of 1 bar.

The pressure profile of the retrieved gas jet, as determined from measurements, shows that the peak pressure decreases exponentially from the point of the gas jet nozzle, as shown in Fig. 6(d). This decay in pressure is more pronounced near the gas catcher, which could be attributed to the enhanced pumping efficiency of the gas catcher. For drive lasers with relatively lower pulse energies, where the focusing geometry is more important to achieve the desired phase-matching conditions, this behavior can be quite crucial. Further, a linear correlation is observed between the peak pressure within the gas jet and the backing pressure, as shown in Fig. 6(e).

These measurements have been performed without higher harmonics being generated, i.e., no plasma is present; thus, the retrieved pressure profile represents the neutral gas density profile without any ionization. Estimating the atomic density within the medium would ideally be matched with the infrared laser field. Instead, we repeat the measurements with a plasma and use the brightness to define the interaction volume. The width of the volume is defined by the $1/e^2$ width relative to the peak plasma brightness, as shown in Figs. 6(a)–6(c).

To ensure accurate registration of the plasma emission, a composite imaging approach was used. The schlieren image was first acquired with the IR drive laser turned off, using only the schlieren illumination system. Then the schlieren illumination was turned off, and a second frame was captured with the IR drive laser on, recording the plasma emission separately. This method prevents saturation of the CCD and ensures that the plasma region is overlaid onto the retrieved gas density profile without interference from the schlieren system. The downside of this approach is that we cannot take changes in the refractive index induced by the IR drive laser, such as temperature changes or ionization effects, into account.

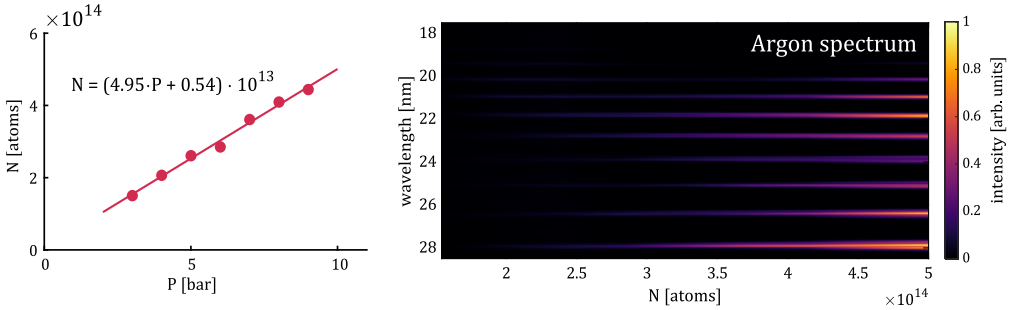

Fig. 7. **Left:** the number of atoms present in the plasma volume grows linearly with the backing pressure. **Right:** the generated higher harmonics in the plasma propagate towards an EUV spectrometer placed downstream. A spectrum is acquired for wavelengths between 18 and 28 nm (equal to harmonic orders 37 and 55) for each backing pressure. Using the schlieren methodology, the intensity per harmonic order can be compared to the number of atoms or gas density within the gas jet rather than the backing pressure, giving a better representation of the source dynamics.

The total amount of argon atoms within the retrieved volume per backing pressure increases linearly with the backing pressure (see Fig. 7), despite the increasing plasma volume. The plasma is located in the center of the gas jet in both x and z, as shown in the outlines in Fig. 6. The generated higher harmonics in the gas jet propagate downstream to the EUV spectrometer after removing the drive laser through grazing incidence plates and aluminum foils, as shown in Fig. 2. The intensity of most higher harmonics between 18 and 28 nm continue to increase with atomic density, with the exception of the higher harmonic orders 41 ($\lambda = 25$ nm), 43 ($\lambda = 24$ nm), and 51 ($\lambda = 20$ nm), which seem to saturate after approximately $4.5 \cdot 10^{14}$ atoms within the defined plasma volume.

5. CONCLUSION

A compact metrology tool, based on schlieren imaging, has been implemented for quantitative retrieval of atomic density profiles in gas jet-based high harmonic generation (HHG) sources. Schlieren imaging offers a simplified approach compared to vibration-sensitive methods such as interferometry. It can serve as a suitable standardized tool in the optimization process of HHG sources. Additionally, this approach allows us to make a fair comparison between different HHG sources, as it directly retrieves the atomic density within the interaction media.

Various gas jet profiles with different backing pressures were retrieved through a double-pass schlieren system with a single spherical mirror with a focal length of 250 mm. The mirror has been illuminated with a 625 nm LED light source, acting as a point source, of which an image was formed outside the vacuum chamber where a knife edge is placed to create a contrast. The schlieren image of the gas jet can be observed with a CCD camera.

As schlieren by itself is not a quantitative approach, some calibration was required. This has been achieved by introducing a known gradient through the use of a weak lens to associate the measured gray values to angular deviations due to refraction by a schlieren object. A deflection angle can be resolved within ± 2.1 mrad with a resolution of 16.5 µrad. After a Radon inversion (or Abel inversion), the jet profile can be retrieved in terms of the refractive index and therefore pressure or atomic density using the Gladstone–Dale relation.

The nozzle in the vacuum system was fed by backing pressures ranging between 2 and 10 bar, where a linear relationship between the peak pressure within the gas jet and its backing pressure was observed. Furthermore, an exponential decay in the peak pressure in the gas jet is observed starting from the nozzle. A steeper drop-off is observed as the flow approaches a vacuum-pumped gas catcher. This indicates the influence of the nozzle and the vacuum system on the shape and behavior of the gas jet and thus shows that comparing gas jet-based sources can be challenging without retrieving the atomic density profile of the gas jet.

The brightness of the produced plasma in the gas jet can serve as a basis for estimating the volume of the medium used in the high harmonic generation process. With the obtained density measurements and volume, the number of atoms present within the interaction volume of the laser field and the medium can be estimated.

While this study focuses on the retrieval of gas density profiles using schlieren imaging, this technique has the potential to aid in optimizing gas jet and catcher geometries. Unlike backing pressure, which can be adjusted experimentally in a straightforward manner, parameters such as nozzle diameter, gas jet shape, and gas catcher design involve a complex analysis of fluid dynamics that is challenging to the model accurately. Schlieren imaging could provide valuable insight into these parameters by enabling direct density measurements. A future study could systematically explore these factors, leveraging the schlieren technique to refine gas jet designs for high harmonic generation applications.

Funding. Nederlandse Organisatie voor Wetenschappelijk Onderzoek (P16-08).

Acknowledgment. The authors would like to thank and acknowledge the associated partners within the LINX program.

Disclosures. The authors declare no conflicts of interest.

Data availability. Data underlying the results presented in this paper are available in Dataset 1, Ref. [67].

Supplemental document. See Supplement 1 for supporting content.

REFERENCES

1. L. Loetgering, S. Witte, and J. Rothhardt, "Advances in laboratory-scale ptychography using high harmonic sources," Opt. Express **30**, 4133–4164 (2022).

2. W. Boutu, M. Ducousso, J.-F. Hergott, *et al.*, "Overview on HHG high-flux sources," in *Optical technologies for extreme-ultraviolet and soft X-ray coherent sources* (Springer, 2015), pp. 63–78.
3. D. Strickland and G. Mourou, "Compression of amplified chirped optical pulses," Opt. Commun. **55**, 447–449 (1985).
4. J. Boullet, Y. Zaouter, J. Limpert, *et al.*, "High-order harmonic generation at a megahertz-level repetition rate directly driven by an ytterbium-doped-fiber chirped-pulse amplification system," Opt. Lett. **34**, 1489–1491 (2009).
5. J. S. Feehan, J. H. Price, T. J. Butcher, *et al.*, "Efficient high-harmonic generation from a stable and compact ultrafast yb-fiber laser producing, 350 fs pulses based on bendable photonic crystal fiber," Appl. Phys. B **123**, 43 (2017).
6. M. Gebhardt, T. Heuermann, Z. Wang, *et al.*, "Soft x-ray high order harmonic generation driven by high repetition rate ultrafast thulium-doped fiber lasers," Proc. SPIE **11260**, 84–89 (2020).
7. M. Tschernajew, S. Hädrich, R. Klas, *et al.*, "High repetition rate high harmonic generation with ultra-high photon flux," in *Laser Applications Conference* (Optica, 2020), paper JTh2A-21.
8. A. Kirsche, M. Gebhardt, R. Klas, *et al.*, "Continuously tunable high photon flux high harmonic source," Opt. Express **31**, 2744–2753 (2023).
9. S. Hädrich, A. Klenke, J. Rothhardt, *et al.*, "High photon flux table-top coherent extreme-ultraviolet source," Nat. Photonics **8**, 779–783 (2014).
10. J. Limpert and J. Rothhardt, "High average power high-harmonic euv sources and high performance imaging at the nanoscale," in *EPJ Web of Conferences* (EDP Sciences, 2024), Vol. **307**, p. 03001.
11. R. Klas, A. Kirsche, M. Gebhardt, *et al.*, "Ultra-short-pulse high-average-power megahertz-repetition-rate coherent extreme-ultraviolet light source," PhotoniX **2**, 1–8 (2021).
12. M. Tanksalvala, C. L. Porter, Y. Esashi, *et al.*, "Nondestructive, high-resolution, chemically specific 3D nanostructure characterization using phase-sensitive EUV imaging reflectometry," Sci. Adv. **7**, eabd9667 (2021).
13. Y. Shao, S. Weerdenburg, J. Seifert, *et al.*, "Wavelength-multiplexed multi-mode EUV reflection ptychography based on automatic differentiation," Light Sci. Appl. **13**, 196 (2024).
14. C. L. Porter, M. Tanksalvala, M. Gerrity, *et al.*, "General-purpose, wide field-of-view reflection imaging with a tabletop 13 nm light source," Optica **4**, 1552–1557 (2017).
15. W. Eschen, L. Loetgering, V. Schuster, *et al.*, "Material-specific high-resolution table-top extreme ultraviolet microscopy," Light Sci. Appl. **11**, 117 (2022).
16. T. T. Luu, M. Garg, S. Y. Kruchinin, *et al.*, "Extreme ultraviolet high-harmonic spectroscopy of solids," Nature **521**, 498–502 (2015).
17. N. Lin, A. J. Den Boef, S. B. Roobol, *et al.*, "HHG source, inspection apparatus and method for performing a measurement," U.S. Patent 10,816,906 (27 October, 2020).
18. J. L. Krause, K. J. Schafer, and K. C. Kulander, "High-order harmonic generation from atoms and ions in the high intensity regime," Phys. Rev. Lett. **68**, 3535–3538 (1992).
19. R. Weissenbilder, S. Carlström, L. Rego, *et al.*, "How to optimize high-order harmonic generation in gases," Nat. Rev. Phys. **4**, 713–722 (2022).
20. P. B. Corkum, "Plasma perspective on strong field multiphoton ionization," Phys. Rev. Lett. **71**, 1994–1997 (1993).
21. C. Altucci, T. Starczewski, E. Mevel, *et al.*, "Influence of atomic density in high-order harmonic generation," J. Opt. Soc. Am. B **13**, 148–156 (1996).
22. J. Grant-Jacob, B. Mills, T. J. Butcher, *et al.*, "Gas jet structure influence on high harmonic generation," Opt. Express **19**, 9801–9806 (2011).
23. A. L'Huillier, K. Schafer, and K. Kulander, "Higher-order harmonic generation in xenon at 1064 nm: the role of phase matching," Phys. Rev. Lett. **66**, 2200–2203 (1991).
24. T. Popmintchev, M.-C. Chen, P. Arpin, *et al.*, "The attosecond nonlinear optics of bright coherent x-ray generation," Nat. Photonics **4**, 822–832 (2010).
25. P. Salieres, A. L'Huillier, and M. Lewenstein, "Coherence control of high-order harmonics," Phys. Rev. Lett. **74**, 3776–3779 (1995).
26. E. Constant, D. Garzella, P. Breger, *et al.*, "Optimizing high harmonic generation in absorbing gases: model and experiment," Phys. Rev. Lett. **82**, 1668–1671 (1999).
27. D. M. Gaudiosi, B. Reagan, T. Popmintchev, *et al.*, "High-order harmonic generation from ions in a capillary discharge," Phys. Rev. Lett. **96**, 203001 (2006).
28. D. E. Couch, D. D. Hickstein, D. G. Winters, *et al.*, "Ultrafast 1 MHz vacuum-ultraviolet source via highly cascaded harmonic generation in negative-curvature hollow-core fibers," Optica **7**, 832–837 (2020).
29. B. Reagan, T. Popmintchev, M. Grisham, *et al.*, "Enhanced high-order harmonic generation from Xe, Kr, and Ar in a capillary discharge," Phys. Rev. A **76**, 013816 (2007).
30. M.-C. Chen, M. R. Gerrity, S. Backus, *et al.*, "Spatially coherent, phase matched, high-order harmonic EUV beams at 50 KHz," Opt. Express **17**, 17376–17383 (2009).
31. B. Vodungbo, A. B. Sardinha, J. Gautier, *et al.*, "Polarization control of high order harmonics in the EUV photon energy range," Opt. Express **19**, 4346–4356 (2011).
32. P.-M. Paul, E. S. Toma, P. Breger, *et al.*, "Observation of a train of attosecond pulses from high harmonic generation," Science **292**, 1689–1692 (2001).
33. R. Klas, W. Eschen, A. Kirsche, *et al.*, "Generation of coherent broadband high photon flux continua in the XUV with a sub-two-cycle fiber laser," Opt. Express **28**, 6188–6196 (2020).
34. N. Burnett, H. Baldis, M. Richardson, *et al.*, "Harmonic generation in CO_2 laser target interaction," Appl. Phys. Lett. **31**, 172–174 (1977).
35. S. Ghimire and D. A. Reis, "High-harmonic generation from solids," Nat. Phys. **15**, 10–16 (2019).
36. T. T. Luu, Z. Yin, A. Jain, *et al.*, "Extreme–ultraviolet high–harmonic generation in liquids," Nat. Commun. **9**, 3723 (2018).
37. S. Karatodorov, R. Lera, M. Raclavsky, *et al.*, "Multi-pass probing for high-sensitivity tomographic interferometry," Sci. Rep. **11**, 15072 (2021).
38. V. Malka, C. Coulaud, J. Geindre, *et al.*, "Characterization of neutral density profile in a wide range of pressure of cylindrical pulsed gas jets," Rev. Sci. Instrum. **71**, 2329–2333 (2000).
39. A. Hansen, D. Haberberger, J. Katz, *et al.*, "Supersonic gas-jet characterization with interferometry and Thomson scattering on the omega laser system," Rev. Sci. Instrum. **89**, 10C103 (2018).
40. S. V. Avtaeva, K. V. Gubin, V. I. Trunov, *et al.*, "Algorithm for supersonic gas jet density profile retrieval from interferometric measurement," J. Opt. Soc. Am. A **36**, 910–917 (2019).
41. A. Comby, S. Beaulieu, E. Constant, *et al.*, "Absolute gas density profiling in high-order harmonic generation," Opt. Express **26**, 6001–6009 (2018).
42. G. Settles, A. Brandt, and J. Miller, "Full-scale schlieren imaging of shock waves for aviation security research," in *8th International Symposium on Flow Visualization* (1998).
43. G. S. Settles and M. J. Hargather, "A review of recent developments in schlieren and shadowgraph techniques," Meas. Sci. Technol. **28**, 042001 (2017).
44. J. H. Gladstone and T. P. Dale, "XIV. Researches on the refraction, dispersion, and sensitiveness of liquids," Philos. Trans. R. Soc. London **153**, 317–343 (1863).
45. G. Ben-Dor and B. T. Whitten, "Interferometric techniques and data evaluation methods for the utias 10 cm × 18 cm hypervelocity shock tube," Technical report (Citeseer, 1979).
46. J. Anderson, "Experimental determination of the Gladstone-Dale constants for dissociating oxygen," Phys. Fluids **12**, 1-57–1-60 (1969).
47. G. Settles, "Schlieren and shadowgraph techniques: visualizing phenomena in transparent media (Springer-Verlag, Berlin, Germany, 2001)," Eur. J. Mech. B **21**, 493 (2002).
48. D. R. Jonassen, G. S. Settles, and M. D. Tronosky, "Schlieren 'PIV' for turbulent flows," Opt. Lasers Eng. **44**, 190–207 (2006).
49. M. Raffel, "Background-oriented schlieren (BOS) techniques," Exp. Fluids **56**, 1–17 (2015).
50. Y. Ishino, N. Hayashi, I. F. Bt Abd Razak, *et al.*, "3D-CT (computer tomography) measurement of an instantaneous density distribution of turbulent flames with a multi-directional quantitative schlieren camera (reconstructions of high-speed premixed burner flames

with different flow velocities)," Flow, Turbul. Combust. **96**, 819–835 (2016).
51. J. P. Couperus, A. Köhler, T. Wolterink, *et al.*, "Tomographic characterisation of gas-jet targets for laser wakefield acceleration," Nucl. Instrum. Methods Phys. Res. A **830**, 504–509 (2016).
52. N. F. Barnes and S. L. Bellinger, "Schlieren and shadowgraph equipment for air flow analysis," J. Opt. Soc. Am. **35**, 497–509 (1945).
53. S. Kook, M. K. Le, S. Padala, *et al.*, "Z-type schlieren setup and its application to high-speed imaging of gasoline sprays," Technical report, SAE Technical Paper (2011).
54. M. Boselli, V. Colombo, E. Ghedini, *et al.*, "Schlieren high-speed imaging of a nanosecond pulsed atmospheric pressure non-equilibrium plasma jet," Plasma Chem. Plasma Process. **34**, 853–869 (2014).
55. J. W. Bradley, J.-S. Oh, O. T. Olabanji, *et al.*, "Schlieren photography of the outflow from a plasma jet," IEEE Trans. Plasma Sci. **39**, 2312–2313 (2011).
56. J. Gerold, P. Vogl, and M. Pfitzner, "New correlation of subsonic, supersonic and cryo gas jets validated by highly accurate schlieren measurements," Exp. Fluids **54**, 1–15 (2013).
57. M. J. Hargather and G. S. Settles, "A comparison of three quantitative schlieren techniques," Opt. Lasers Eng. **50**, 8–17 (2012).
58. F. Salehi, A. Goers, L. Feder, *et al.*, "Characterization of a 100 micrometer-scale cryogenically cooled gas jet for near-critical density laser-plasma experiments," Rev. Sci. Instrum. **90**, 103001 (2019).
59. D. Kaganovich, D. Gordon, M. Helle, *et al.*, "Shaping gas jet plasma density profile by laser generated shock waves," J. Appl. Phys. **116**, 013304 (2014).
60. U. Kogelschatz and W. Schneider, "Quantitative schlieren techniques applied to high current arc investigations," Appl. Opt. **11**, 1822–1832 (1972).
61. A. K. Agrawal, B. W. Albers, and D. W. Griffin, "Abel inversion of deflectometric measurements in dynamic flows," Appl. Opt. **38**, 3394–3398 (1999).
62. Y. Xiong, T. Kaufmann, and N. Noiray, "Towards robust BOS measurements for axisymmetric flows," Exp. Fluids **61**, 178 (2020).
63. E. Traldi, M. Boselli, E. Simoncelli, *et al.*, "Schlieren imaging: a powerful tool for atmospheric plasma diagnostic," EPJ Techn. Instrum. **5**, 1–23 (2018).
64. D. J. Tan, D. Edgington-Mitchell, and D. Honnery, "Measurement of density in axisymmetric jets using a novel background-oriented schlieren (BOS) technique," Exp. Fluids **56**, 1–11 (2015).
65. A. C. Kak and M. Slaney, *Principles of Computerized Tomographic Imaging* (SIAM, 2001).
66. Matlab, "Radon transform mathworks," (2024) accessed on 2 January 2024, https://nl.mathworks.com/help/images/ref/radon.html.
67. S. Weerdenburg, R. Horsten, and W. Coene, "COMSOL simulation—gas jet in vacuum system HHG," figshare (2025), https://doi.org/10.6084/m9.figshare.28425995.